Accepted Manuscript

ROYAL SOCIETY
OF CHEMISTRY

rsc.li/es-nano

Spectral Characterization and Surface Complexation Modeling of Low Molecular Weight Organics on Hematite Nanoparticles: Role of Electrolytes in the Binding Mechanism

Arthur Situm[a], Mohammad A. Rahman[a], Sabine Goldberg[b], and Hind A. Al-Abadleh[a]*

[a]Department of Chemistry and Biochemistry, Wilfrid Laurier University,

Waterloo, ON N2L 3C5, Canada

[b]USDA-ARS, U.S. Salinity Laboratory, Riverside, CA 92507, USA

_____

* Corresponding author phone: (519)884-0710, ext.2873; fax: (519)746-0677; e-mail:
halabadleh@wlu.ca.

Nano Impact

Owing to their unique reactivity with organic matter, ubiquity in environmental systems and increased use in medical research, hematite nanoparticles have been the focus of this study, which aims at understanding their surface chemistry with low molecular weight organics under environmentally- and biologically- relevant conditions. The molecular-level details from spectral analysis of surface species led to the development of thermodynamic models based on binding mechanisms. A deeper understanding of organic molecules at the aqueous solution-hematite nanoparticle interface can lead to better predictions of environmental fate and reactivity of nanoparticles and pollutants, and also design of medical devices and drugs.

Abstract

Given the ubiquity of organic-metal oxide interfaces in environmental and medical systems, it is incumbent to obtain mechanistic details at the molecular level from experimental procedures that mimic real systems and conditions. We report herein the adsorption pH envelopes (range 9-5), isotherms at pH 7, and H/D exchange spectra using attenuated total internal reflectance Fourier transform infrared spectroscopy (ATR-FTIR) for citrate, oxalate and pyrocatechol on hematite nanoparticles. Experimental data were coupled with the application of triple layer surface complexation models derived for each organic compound based on the interpretation of spectral data. These studies showed that the structure of the organic species influences the type and relative amounts of inner- versus outer-sphere surface complexes. This has consequences on surface charge as shown from electrolyte concentration-dependent studies. For example, citrate forms a mix of protonated monodentate inner-sphere complexes with one negative charge and deprotonated outer-sphere complexes with *net* two negative charges. Oxalate forms mostly doubly deprotonated outer-sphere complexes with inaccessible neighboring site with contributions from deprotonated inner-sphere complexes. And lastly, pyrocatechol forms mostly bidentate inner-sphere complexes. Layering of interfacial electrolyte ions from KCl, NaCl and KBr, used to adjust the electrolyte concentration caused an overall enhancement in the amount adsorbed of weakly-bonded citrate and oxalate. Also, hematite nanoparticles retain more adsorbed citrate and pyrocatechol than adsorbed oxalate when flowing chloride or bromide as negatively-charged weak desorbing agents at pH 7. These results have implications on the overall surface chemistry of hematite nanoparticles in the presence of organic matter, particularly those containing carboxylate and phenolate functional groups.

Introduction

Organics at the metal oxide/mineral interface have been the subject of extensive investigations given their importance to many environmental, biological and medical systems.[1-9] In general, the interactions of organic matter with metal oxides and minerals occur via a number of mechanisms that include chelation, ligand exchange, electrostatic, van der Waals and hydrophobic interactions, cation bridging and hydrogen bonding.[3] These processes lead to changes in surface charge and functional groups, hydrophobicity, interfacial water structure, adhesion strength, and dissolution of the metal oxide/mineral phase.[10-18] Despite the wealth of knowledge on the interactions of organics with metal oxide and mineral particles generated mostly from ex-situ bulk batch measurements, molecular-level details of these interactions from *in situ* measurements are limited. Increasingly, recent work in this area has focused on identifying the type of surface organic functional groups, their concentrations, and distribution relative to the mineral phase using techniques such as attenuated total internal-reflectance spectroscopy (ATR-FTIR)[19-26], scanning transmission X-ray microscopy–near edge X-ray absorption fine structure spectroscopy (STXM-NEXAFS) and extended X-ray absorption fine structure spectroscopy (EXAFS).[27,28]

The focus of this study is on the surface chemistry of hematite nanoparticles, given their unique chemistry in environmental processes[5,29] and medical applications[6,8] with three types of model low molecular weight organic compounds: citric and oxalic acids and pyrocatechol. These organics represent simple aliphatic and aromatic compounds that will influence the charge and hydrophilicity of the interface to varying degrees upon adsorption. The structure of surface organic molecules on iron-(oxyhydr)oxides and iron-containing clays and oxides (mostly goethite and ferrihydrite) has been investigated using transmission and ATR-FTIR.[19-23,30]

Throughout this study, the terms 'inner-sphere' and 'outer-sphere' are used to describe surface complexes per the definitions reported by Stumm.[31,32] Inner-sphere complexes refer to molecules forming a direct covalent bond or bonds with surface sites through chemisorption, and outer-sphere complexes refer to those experiencing electrostatic or weak van der Waals interactions with the surface (i.e., physisorption). Kubicki *et al*.[20] reported that chemisorption of carboxylic acids that include citric and oxalic acids onto clays is limited without the presence of Fe-hydroxides within the clay matrix. Wells and co-workers[21] reported spectra of adsorbed citrate on goethite as a function of pH and compared them to those collected for aqueous phase species. They suggested the formation of inner-sphere complexes at pH 4.6 and 7 via one or more carboxyl groups, and outer-sphere complexes at pH 8.8. Further examination of the adsorption of citric acid on goethite aqueous suspensions was carried by Persson and co-workers[22] using 2-D correlation spectroscopy formalism. This spectral analysis method identified a protonated adsorbed citrate complex involving only carboxylate coordination at low pH, and an inner-sphere complex at high pH coordinated via a combination of hydroxyl and carboxylate groups. At circumneutral pH, an outer-sphere complex was also identified. More recently where metal oxide and clay samples were allowed to equilibrate with citric acid solutions at pH 6, Yeasmin *et al*.[23] reported that citric acid forms a mixture of monodentate inner-sphere and outer-sphere complexes with ferrihydrite and goethite based on the spectral analysis of ATR-FTIR data. By means of batch experiments, varying the electrolyte concentration over the range 1-500 mM using $NaNO_3$ and the pH range 7.5-3 was found to have little effect on the amount of adsorbed citrate on goethite.[30] This finding was interpreted to indicate strong binding mechanism that leads to minimizing the charge of the diffuse double layer (DDL). This has consequences on

reversing the charge of goethite particles particularly at pH values below the point of zero charge due to high surface coverage of negatively charged adsorbed citrate.

The structure of adsorbed oxalate was also studied by a number of groups.[23,30,33] Similar to the ATR-FTIR studies done on citric acid adsorption, Yeasmin *et al*.[23] reported that oxalate forms a mixture of bidentate inner-sphere and outer-sphere complexes with ferrihydrite and goethite at pH 6. Filius *et al*.[30] reported inner-sphere bidentate binuclear complexes for oxalate on goethite. The amounts adsorbed oxalate were found to be suppressed upon increasing electrolyte concentration by Mesuere and Fish.[34] Persson and co-workers[28,33] coupled ATR-FTIR with EXAFS to examine the water-goethite interface upon oxalate complexation as a function of pH. They found that oxalate forms both inner- and outer-sphere complexes over a broad pH range, and that the former is a stable five-membered ring bidentate mononuclear complex. Similar conclusions were made by Cwiertny *et al*.[17] for the adsorption of oxalic acid on goethite micro- and nanorods at pH 3 with more outer-sphere on the smaller size particles. This observation was attributed to the larger density of surface hydroxyl groups on goethite nanorods.

The adsorption of aqueous phase pyrocatechol on hematite[24] and goethite[25] particles at neutral to basic pH was studied using ATR-FTIR and batch experiments. Gulley-Stahl *et al*.[24] found that adsorbed pyrocatechol promoted dissolution of Fe_2O_3 under neutral and basic conditions, compared to proton-driven dissolution that is significant under acidic conditions (pH < 5). This was explained by the formation of inner-sphere pyrocatechol complexes at pH > 5 with a higher degree than outersphere complexation under acidic conditions. It was inferred that bidentante mononuclear complexes at pH > 5 are responsible for promoting dissolution since other studies showed that binuclear bidentate complexes of pyrocatechol inhibit dissolution.[35-37] Yang *et al*.[25] studied pyrocatechol adsorption on goethite particles using ATR-FTIR and

complemented these measurements with density functional theory (DFT) calculations. A number of complexes were considered: mononuclear monodentate (M-M), binuclear bidentate (B-B) and mononuclear bidentate (M-B). The time profile of spectral features assigned to these complexes revealed that M-M and B-B complexes co-exist in the pH range 5-9, with the possibility of partial conversion of M-M to B-B via proton exchange with neighboring surface sites under basic conditions and high surface coverage. Undetectable dissolution of goethite (*i.e.* $[Fe]_{soluble} < 5$ μg L^{-1}) was reported in the presence and absence of pyrocatechol for 12 hr in the dark under neutral to basic pH. This finding was explained by the dominance of B-B complexes that inhibit dissolution under these conditions, and the possibility for dissolution-readsorption as observed in oxalate-goethite systems.

On the mathematical modeling side of the binding thermodynamics, surface complexation models (SCMs) have been used previously to describe the adsorption of organic species on oxide minerals.[30,34,38-42] Citric acid adsorption was described with the constant capacitance mode (CCM) on the aluminum oxide, pseudoboehmite, using three monodentate inner-sphere surface complexes.[40] On goethite, tridentate and tetradentate inner-sphere surface complexes were used to describe citrate adsorption using the charge distribution multisite complexation model (CD-MUSIC).[30] Oxalate adsorption on goethite has been described with the triple layer model (TLM)[39,42], the DLM[34], and the CD-MUSIC model.[30] Early modeling studies chose monodentate outer-sphere surface complexes for oxalate adsorption based on quality-of-fit criteria.[34,39] More recent investigations defined bidentate inner-sphere surface complexes based on infrared spectroscopic evidence.[30,42] The adsorption of pyrocatechol was described using CCM on hydrous γ-Al$_2$O$_3$[38] and using the diffuse layer model (DLM) on goethite.[41] In both cases, inner-sphere monodentate surface complexes were used.

The aforementioned variability in the type of organic surface complexes motivated the current study, where we provide detailed spectral analysis of the binding mechanism of citrate, oxalate, and pyrocatechol to hematite nanoparticles from pH-, electrolyte concentration-, and concentration-dependent adsorption studies using *in situ* ATR-FTIR in *the flow mode*. These adsorption studies were followed by flow mode *desorption* using chloride and bromide as desorbing agents under the same experimental settings. The triple layer SCM was customized to each type of organic surface complexes to obtain thermodynamic binding constants based on the interpretation of the spectroscopic data presented herein. Results show that *flow mode* experiments amplify the effect of interfacial electrolyte layering leading to an enhancement in outer-sphere complexation with increasing electrolyte concentration for some organics. This effect was not observed previously on goethite samples from bulk batch experiments as a function of electrolyte concentration. The significance of these findings is discussed in terms of their relevance to natural and biological environments.

Experimental methods

Chemicals

Solutions were made by dissolving respective compounds in KCl solution (potassium chloride, ACS grade, 99.0%+, EMD) prepared fresh in 18 MΩ-cm Millipore water and finally adjusted to the desired concentration and pH by using dilute and concentrated solutions of HCl (hydrochloric acid, 6 N, Ricca Chemical Company) and NaOH (sodium hydroxide, GR ACS, 99.0-100%, EMD). Experiments with NaCl (sodium chloride, 99%, ACS reagent, BDH) and KBr (potassium bromide, anhydrous, 99%+, ACS reagent, Sigma-Aldrich) were also performed. For H/D exchange experiments, these solutions were prepared in liquid D_2O (deuterium oxide,

99.9 atom %D, Sigma-Aldrich) and adjusted to the desired pD using NaOD (sodium deuteroxide,
40 wt.% solution). Powder of organic compounds used herein (as received without further
purification) include citric acid monohydrate ($C_6H_8O_7 \cdot H_2O$, 99%+, ACS reagent, Alfa Aesar),
oxalic acid (Oxalic acid dihydrate, 99%+, ACS reagent, Sigma-Aldrich), pyrocatechol (99%+,
Sigma-Aldrich), iron (III) oxalate hexahydrate ($Fe_2(C_2O_4)_3 \cdot 6H_2O$, technical grade, Sigma-
Aldrich), iron(III) citrate ($C_6H_5FeO_7$, technical grade, Sigma-Aldrich), sodium hydrogen
carbonate ($NaHCO_3$, ACS Specifications, Caledon) and iron(III) chloride hexahydrate
($FeCl_3 \cdot 6H_2O$, CAS Registry Number 10025-77-1, Sigma-Aldrich). All solutions were prepared
freshly before the start of each experiment and were covered with parafilm until used. Hematite
nanoparticles (α-Fe_2O_3, 98+%, US Research Nanomaterials, Inc, batch US3180) were
characterized for these experiments to obtain BET surface area (N_2 gas, 54 ± 5 m^2 g^{-1}, Aveka Inc.),
isoelectric point (IEP) (zeta potential titration, 8.45, Aveka Inc.), and particle shape and size
(TEM Philips C12 at 120 keV, spherical, 39 ± 11 nm average spherical diameter, Canadian Centre
for Electron Microscopy, McMaster University). Figs. S1 and S2 in the Electronic
Supplementary Information (ESI) show the TEM images and zeta potential measurements of
hematite nanoparticles. All solutions were prepared in open air where samples were in
equilibrium with atmospheric CO_2 to ensure results reported herein are applicable and relevant to
physical processes in real life environmental and biological systems. The interference of the
infrared signal assigned to surface carbonate was investigated in control experiments using high
purity N_2 gas as shown below in section B.

A film was prepared using 6 mg of hematite nanoparticles in a 1.30 mL water-ethanol
[0.91:0.39 (v/v)] mixture. The mixture was ultrasonicated (default power, Fisher Scientific
Mechanical Ultrasonic Cleaner FS20) for one hour and the slurry obtained was deposited on a

dry ZnSe ATR crystal. The deposited film was allowed to dry for 12-18 hours in air at room temperature (23± 2 °C) under an Al-foil tent on the lab bench. The thickness of the hematite film deposited on the ZnSe ATR crystal was measured by depositing the same amount (6 mg) of the hematite nanoparticles slurry on a glass slide with similar dimensions using an ultra fast optical profiler (Wyko NT 3300 Series, 7.5±1.4 μm, Electrochemical Technology Centre, University of Guelph). This thickness along with area covered by the film (7.2 cm^2) was used to calculate the bulk density of hematite nanoparticles film (1.1 g cm^{-3}). Aqueous solutions were flowed at a rate of 2 mL min^{-1} across the ATR flow cell using Tygon tubes (0.8 mm I.D., Masterflex) and a compact pump (Masterflex L/S).

ATR-FTIR spectroscopy experiments

ATR-FTIR spectra were collected as a function of time on a freshly prepared hematite nanoparticles film using a HATRPlus accessory (Pike Technologies) installed in a Nicolet 8700 FTIR spectrometer (Thermo Instruments) equipped with a liquid N_2-cooled MCT detector. The ATR flow cell used in the experiments contains either a 45° Ge or 60° ZnSe internal reflection element (IRE, 80×10×4 mm) with volumes of 500 and 100 μL, respectively. The Ge flow cell was used for collecting aqueous phase spectra at pH 2, 4 and 8 for citric and oxalic acids. All other aqueous phase spectra at pH 7 were collected using the ZnSe flow cell. Typically, single beam ATR-FTIR spectra were collected at 8 cm^{-1} resolution with 100 averaged scans throughout the experiments. Bulk phase experiments were conducted for standard solutions of the organic compounds listed above at room temperature. A single beam spectrum was collected first for the background solution (0.01 M KCl in H_2O at a given pH). This was followed by flowing the

standard solution of the compound of interest at a rate of 2 mL min^{-1} for 10 min before collecting

a single beam spectrum by averaging 100 scans.

Each pH envelope experiment was conducted on a freshly-prepared film by first flowing

background KCl solution at pH 7 for 60 min followed by KCl at pH 9 for 30 min and collection

of the single beam spectrum. Then, flow of 0.1 mM standard solution of each organic compound

started, which was adjusted to the desired pH in the range 9-5 starting with the basic pH and

lowered 0.5 pH units by concentrated HCl. Single beam spectra of the surface upon flowing the

solutions were collected after 30 min equilibrium time by averaging 100 scans. For each pD

experiment, background KCl solution at pD 7 was flowed for 10 min at a 1 mL/min flow rate,

followed by KCl at pD 8 or 9 for 10 min and collection of the single beam spectrum. Then, flow

of 0.1 mM standard solution of each organic compound at pD 8 or 9 started for 10 min, followed

by solutions adjusted to pD 7, 6, 5 and 4, respectively, each for 10 min at a 1 mL/min flow rate.

In these experiments, the pH and pD were constantly monitored through a pH and pD meters

inserted in the solution beaker.

For each isotherm experiment, solutions of a given organic compound were flowed from

lower to higher concentrations across the freshly prepared hematite film for 30 min for each

concentration. Longer equilibrium times up to 1 hr were found to cause little change in the

absorbance of the most intense spectral feature attributed to surface species. At the beginning of

every experiment, the KCl solution was flowed first for 90 min to record background spectra.

Each single beam spectrum collected at the end of passing every organic compound solution at a

given concentration was referenced to the last one recorded for the background solution to obtain

the absorbance spectra reported herein. In these experiments, the pH was constantly monitored

through a pH meter inserted in the solution beaker. All the experiments were repeated 4-6 under

the same experimental conditions to determine the reproducibility of our results. Calculations of surface coverage in units of molecules·cm^{-2} from ATR-FTIR spectra are described in the ESI. According to these calculations, the maximum adsorption capacity of the hematite nanoparticles at pH 7 and 0.01 M of each organic was found to be $(2\pm0.5)\times10^{13}$, $(1\pm0.3)10^{13}$, and $(5\pm1.3)\times10^{13}$ molecule·cm^{-2} for citrate, oxalate and pyrocatechol, respectively.

Surface complexation modeling (SCM)

The triple layer SCM[43] was used to describe the adsorption of citric and oxalic acids, and pyrocatechol onto hematite nanoparticles. In the present model application, the following organic surface complexation constants were considered for citric acid (CA), oxalic acid (OA) and pyrocatechol (PC), respectively:

$$FeOH + H_3CA \leftrightharpoons FeHCA^- + H^+ + H_2O \tag{1}$$

$$FeOH + H_3CA \leftrightharpoons FeOH_2^+ - CA^{3-} + 2H^+ \tag{2}$$

$$2FeOH + H_2OA \leftrightharpoons FeOH(FeOH_2^+) - OA^{2-} + H^+ \tag{3}$$

$$FeOH + H_2OA \leftrightharpoons FeOA^- + H^+ + H_2O \tag{4}$$

$$2FeOH + H_2PC \leftrightharpoons Fe_2PC + 2H_2O \tag{5}$$
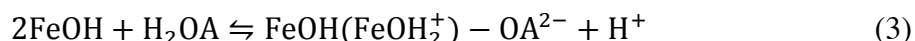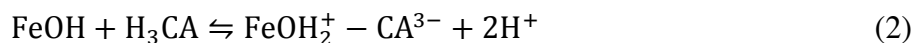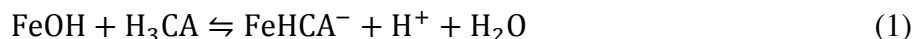
where FeOH represents reactive surface hydroxyl groups on the hematite nanoparticles surface. The SCM used herein contains additional reactions and mathematical expressions for equilibrium constants that describe the clean surface and organic species in the bulk as shown in the ESI. Even though the surface complexation reactions are written starting with the completely undissociated acids, the model application contains the aqueous speciation reaction(s) for CA, OA and PC. Equilibrium constant expressions for the organic surface complexation constants are:

$$K_{CA}^1(int) = \frac{[FeHCA^-][H^+]}{[FeOH][H_3CA]}\exp(-F\psi_o/RT) \qquad (6)$$

$$K_{CA}^2(int) = \frac{[FeOH_2^+ - CA^{3-}][H^+]^2}{[FeOH][H_3CA]}\exp[F(\psi_o - 3\psi_\beta)/RT] \qquad (7)$$

$$K_{OA}^1(int) = \frac{[FeOH(FeOH_2^+) - OA^{2-}][H^+]}{[FeOH]^2[H_2OA]}\exp[(F\psi_o - 2\psi_\beta)/RT] \qquad (8)$$

$$K_{OA}^2(int) = \frac{[FeOA^-][H^+]}{[FeOH][H_2OA]}\exp(-F\psi_o/RT) \qquad (9)$$

$$K_{PC}(int) = \frac{[Fe_2PC]}{[FeOH]^2[H_2PC]} \qquad (10)$$

where F is the Faraday constant (C mol_c^{-1}), ψ is the surface potential (V), R is the molar gas constant (J mol^{-1} K^{-1}), T is the absolute temperature (K), and square brackets indicate concentrations (mol L^{-1}). The exponential terms can be considered as solid phase activity coefficients correcting for the charge on charged surface complexes.

The computer program FITEQL 4.0[44] was used to fit the citrate, oxalate and pyrocatechol surface complexation constants to the experimental adsorption data. This program uses a nonlinear least-squares optimization routine to fit equilibrium constants to experimental data and contains the triple layer SCM of adsorption. To describe adsorption, we relied on the spectral interpretation provided in this study (see Results and Discussion section) in writing equations (1)-(5): (for CA) one protonated inner-sphere with one negative charge surface complex and one deprotonated outer-sphere with net 2 negative charges surface complex, (for OA) one doubly-deprotonated outer-sphere with inaccessible neighboring site surface complex, and one inner-sphere mononuclear bidentate surface complexe, and (for PC) one inner-sphere binuclear bidentate surface complex.

14

Results and discussion

In this paper, results are presented in three main sections: (A) Speciation and spectral analysis of the organics in the bulk aqueous phase; (B) Spectral characterization of surface organics as a function of pH, pD and electrolyte concentration; and (C) Thermodynamic analysis using triple layer SCM of adsorption isotherms and pH envelopes.

(A) Speciation and spectral analysis of the organics in the bulk aqueous phase

To aid in the interpretation of the organic surface complexes on hematite nanoparticles, it is informative to examine the spectra of organics in the aqueous phase as function of pH and upon complexing with soluble Fe(III). Fig. 1 shows ATR-FTIR absorbance spectra for citric acid (left) and oxalic acid (right) along with spectra of standard solutions of iron citrate and iron oxalate at pH 7. Similar spectra were collected for pyrocatechol in reference [45], which are also shown in Fig. S3. Changes in the peak intensities and location as a function of pH is explained by the different chemical species dominant at that specific pH based on the speciation curves shown in Fig. S4. The assignment of the peaks to each chemical species is listed in Table 1. As referenced in the table, similar spectra were collected and analyzed in detail by a number of research groups, albeit at other pH values or different concentrations of soluble Fe(III). Briefly, for both citric and oxalic acids, the location and degree of separation, $\Delta \nu$, between symmetric and asymmetric stretching modes of $-CO_2$ functional groups, $\nu(CO_2)$, is sensitive to the degree of protonation and coordination to metal cations.[46] Citric acid at pH 2 and 4 contains three and two $-CO_2H$ groups, respectively, with $\nu(CO_2)$ at 1226 cm^{-1}. This mode nearly disappears at pH 7 where a mixture of fully deprotonated and singly-deprotontated species co-exist at ratio of 80/20. This mode neither exists in the spectrum of citrate complexed with Fe(III) at pH 7 in 1:1 or 1:2
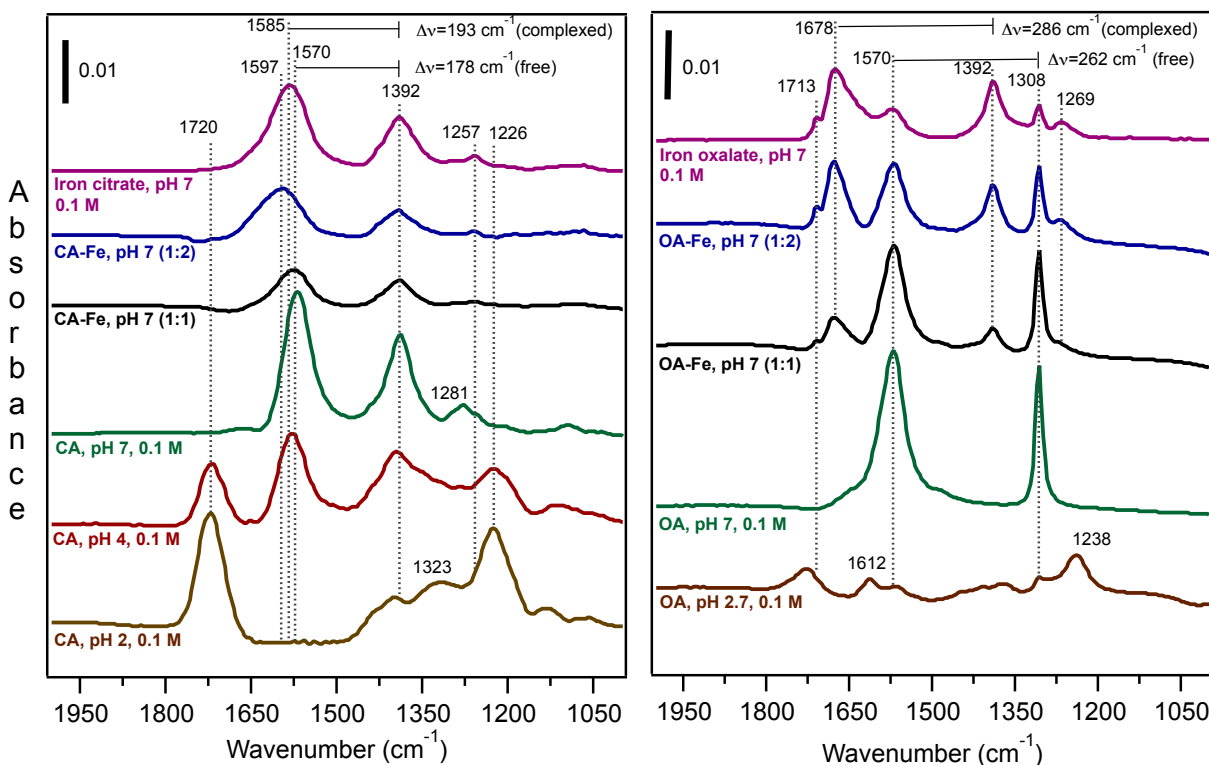
Fig. 1: ATR-FTIR absorbance spectra of solutions containing: (Left, from bottom) citric acid (CA) as a function of pH, CA mixed with $FeCl_3$ with final concentrations of 0.025 M for the 1:1 (mol/mol), and 0.025:0.05 M for the 1:2 (mol/mol) solutions at pH 7. The top spectrum is for iron citrate at pH 7. (Right, from bottom) oxalic acid (OA) as a function of pH, OA mixed with $FeCl_3$ with final concentrations of 0.083 M for the 1:1 (mol/mol), and 0.083:0.17 M for the 1:2 (mol/mol) solutions at pH 7. The top spectrum is for iron oxalate at pH 7. The dominant chemical species and the assignment of the spectral features are listed in Table 1.

molar ratios, nor in the spectrum of iron citrate at pH 7. Because of the sensitivity of this spectral feature to protonation, it was used as a probe to the degree of protonation of surface citric acid on TiO_2 nanoparticles.[47] Similarly, the spectra of oxalic acid at pH 1.5 (ref. [48]) and 2.7 (this work) show a peak at 1238 cm^{-1} assigned to the $\nu(CO_2H)$ groups in fully protonated and singly deprotonated species. This peak disappears in the spectrum of oxalate complexed with Fe(III) at pH 7 in 1:1 or 1:2 molar ratios, and in the spectrum of iron oxalate at pH 7 as detailed below.

Table 1: Assignment of vibrational modes of chemical species of organics from ATR-FTIR spectra shown in Figs. 1, 2.

Chemical Species	Vibrational mode (cm^{-1})							
Citric Acid (CA)	$\nu_a(CO_2^-)$	$\nu_s(CO_2^-)$	$\nu(CO_2H)$ $+\delta(CO_2H)$	$\nu(C=O)$	$\delta(CH_2)$	$\delta(CO_2^-)$	$\nu(CO_2Fe)$	Refs
$H_5C_3O(CO_2H)_3$ (aq), pH 2			1226	1720	1436 [b]	1323		a
$[H_5C_3O(CO_2H)_2(CO_2)]^-$(aq) pH 4	1585	1392	1226	1720	1436 [b]			a
$[H_5C_3O(CO_2)_3]^{3-}$ (aq)/ $[H_5C_3O(CO_2H)(CO_2)_2]^{2-}$(aq) (80/20) pH 7 [c]	1570	1392			1436 [b]	1281		a
Fe-$[H_5C_3O(CO_2)_3]$ (aq) (1:1), pH 7 [d]		1392			1436 [b]		1608 [f]	a
Fe-$[H_5C_3O(CO_2)_3]$ (aq) (1:2), pH 7 [d]		1392			1436 [b]		1616 [f]	a
Fe-$[H_5C_3O(CO_2)_3]$ (aq) pH 7 [e]		1392			1436 [b]		1585	a
Adsorbed CA on hematite nanoparticles	1558 [f] 1535 [f]	1454 [f] 1404 [f] 1365 [f]	1238 [f]	1713 [f]			1616 [f] 1581 1420 [f]	a

Oxalic Acid (OA)	$\nu_a(CO_2^-)$	$\nu_s(CO_2^-)$	$\nu(CO_2H)$ $+\delta(CO_2H)$	$\nu(C=O)$	$\nu(CO_2Fe)$	Refs
$H_2C_2O_4$/ $HC_2O_4^-$ (aq) (50/50) pH 1.5	1625		1238	1722	-	[48]
$C_2O_4^{2-}$/$HC_2O_4^-$ (aq) (15/85), pH 2.7	1612 1570	1308	1238	1728	-	g
$C_2O_4^{2-}$ (aq), pH 7	1570	1308	-	-	-	g
$[Fe-C_2O_4]^+$ (aq) (1:1), pH 7 [h]	1570	1308	-	1713	1678 1392 1269	g
$[Fe-C_2O_4]^+$ (aq) (1:2), pH 7 [h]	1570	1308	-	1713	1678 [h] 1392 [h] 1269 [h]	g
$Fe_2(C_2O_4)_3$ (aq) pH 7 [i]	1570	1308	-	1713	1678 1392 1269	g
$Fe_2(C_2O_4)_3$ (s)	1614	1348	-	1732	1666 1384 1264	[49]
Adsorbed OA on hematite nanoparticles	1647	1427		1697 [f] 1689 [f] 1686 [f]	1670 1288	g

Pyrocatechol (PC)	$\nu(CC)$ +$\nu(CO)$	$\nu(CC)$ +$\delta(CH)$	$\nu(CC)$ +$\delta(OH)$	$\nu(CO)$ +$\delta(CH)$	$\delta(OH)$, $\nu(CO)$	$\delta(CH)$	$\nu(COFe)$	Refs
$H_6C_6O_2$ (aq), pH 4	1600	1516 1473	1377	1277 1261	1200	1103 1038		[45]
$[H_5C_6O_2]^-$ (aq), pH 10	1600	1489	1365	1284 1257 1226		1103 1030		[45]
$[Fe-H_5C_6O_2]^{2+}$ or a mix of $[Fe-H_4C_6O_2]^+/H_6C_6O_2$ (aq) (1:1), pH 4		1516	1377	1277	1200	1103 1026	1477 1254	[45]
$[Fe-H_4C_6O_2]^+$ (1:1), pH 10						1103 1026	1481 1254	[45]
Adsorbed PC on hematite nanoparticles	1601		1386[e]	1281[e]		1103	1489[e] 1477[e] 1258	[j]

Notes: [a] This work with assignments based on references [20-23,47]. [b] not resolvable in Fig. 1 due to broadness of peak centered at 1392 cm^{-1}. [c] Similar spectrum was observed at pH 8. [d] Solution was prepared by mixing citric acid with $FeCl_3$ (aq) at the specified pH and molar ratio. [e] Solution was prepared from powder iron(III) citrate. [f] See Figs. 2, S4, S8 and S9 as a result of spectral subtraction described in text. [g] This work with assignments based on references [17,33,48,49] [h] Increasing the molar ratio of Fe increases the intensity of these peaks suggesting higher concentration of $[Fe-C_2O_4]^+$ (aq). [i] Solution was prepared from powder iron(III) oxalate. [j] This work with assignments based on references [24,25,45].

Higher frequency peaks above 1240 cm^{-1} are mostly assigned to the symmetric (s) and asymmetric (as) $\nu(CO_2^-)$ (1630-1280 cm^{-1}) with contributions from the bending modes (δ) of –CH_2 and –CO_2^- functional groups (Table 1). The value of $\Delta\nu$ for complexed ligands is usually compared with that of free ligands to delineate the type of coordination in the solid phase.[46,50] For example, in the case of the low symmetry ligand acetate, $\Delta\nu = 153$ cm[-1] for the free ion, and shifts to 112 and 185 cm^{-1} in monodentate and bidentate binuclear complexes with Ni(II) and Cu(II), respectivley.[50] This value is even larger in monodentate complexes with Co(III) at 223 cm^{-1} due to the higher formal charge of the central metal.[50] As for the citrate ligand in the *aqueous phase*, the spectra in Fig. 1 (right) show that $\Delta\nu = 178$ and 193 cm^{-1} for free and complexed citrate at pH 7. This 15 cm^{-1} blue shift in $\Delta\nu$ is due to the growth of new spectral components assigned to $\nu(CO_2Fe)$ that arise due to complexation. To isolate these components,

normalized spectrum of *free* citrate solution at pH 7 was subtracted from that of citrate *complexed* to soluble Fe(III) at pH 7. Fig. S5 shows the result of that procedure, where new peaks appeared at 1616 and 1608 cm^{-1} for the 1:2 and 1:1 molar ratios, respectively. The absence of the carbonyl stretching mode, ν(C=O), around 1720 cm^{-1} from the spectra of *complexed* citrate suggests a bidentate mononuclear binding mode. Also, the spectra of *complexed* citrate to soluble Fe(III) at 1:2 and 1:1 molar ratios closely resemble that collected from a standard solution of solid iron(III) citrate at pH 7 (Fig. 1, left), which contains a 1:1 molar ratio of Fe to the citrate ligand. This highlights structural similarities between complexes of iron(III) citrate obtained from either mixing citric acid with soluble Fe(III) or from a standard powder.

The spectra collected for oxalate complexed to soluble Fe(III) at pH 7 in Fig. 1 (right) show clearly distinguishable spectral features at 1678, 1392, and 1269 cm^{-1} assigned to ν(CO$_2$Fe) with $\Delta\nu$ = 286 cm^{-1} compared to 262 cm^{-1} in free oxalate at pH 7. Increasing the molar ratio of Fe(III) increases the intensity of these new features further supporting their assignment above. When compared to the spectrum of a standard solution of iron(III) oxalate at pH 7, the location of the peaks align very well with those obtained from mixing oxalate with soluble Fe(III). However, the relative intensities of the peaks vary, which could be explained by the relative amounts of Fe(III) to the oxalate ligand. In the standard solution, the molar ratio is 2:3 based on the chemical formula shown in the experimental section above. Edwards and Russell[49] analyzed the IR spectrum of solid iron(III) oxalate and proposed the structure shown in Fig. S6. It is likely that this structure is maintained in the aqueous phase at pH 7, hence explaining the apparent differences in intensities of peaks relative to the spectra collected for 1:1 and 1:2 oxalate:Fe(III) molar ratios at pH 7 (Fig. 1, right). Persson and Axe[33] performed detailed structural analysis of

the aqueous phase complex of 3:1 molar ratio oxalate:Fe(III) and concluded that oxalate moieties

form stable five-membered ring mononuclear bidentate complexes with Fe(III). Hence, it is very

likely that at pH 7, oxalate forms a similar complex with Fe(III) in solutions containing 1:1 and

1:2 molar ratios.

Moreover, Table 1 lists the assignments of spectral features observed in the ATR-FTIR

spectra[45] of pyrocatechol as a function of pH, with and without soluble Fe(III). The chemical

species shown with no Fe(III) are based on the speciation curve of pyrocatechol shown in Fig.

S4c. Detailed spectral analysis was provided in our earlier work[45], which basically highlighted

the changes to the number and location of spectral features assigned to aromatic ν(CC) and

ν(CO) upon deprotonation and complexation with Fe(III). Briefly, under acidic conditions (pH

4) where fully protonated pyrocatechol is the dominant species, the maximum number of features

is observed. Adding soluble Fe(III) to obtain a 1:1 molar ratio solution does not change the

number of peaks, but red shifts the peak at 1261 cm^{-1} to 1254 cm^{-1} accompanied by an increase in

intensity. Under basic conditions (pH 10), the ν(CC), with contributions from the δ(CH),

appears as a singlet peak at 1489 cm^{-1}, which red shifts to 1481 cm^{-1} when Fe(III) is present.

Also, at pH 10, the features assigned to ν(CO) with contributions from the δ(CH) appear at 1284,

1257 and 1226 cm^{-1}, which combine into an intense singlet at 1254 cm^{-1} when Fe(III) is added.

Another effect of complexing to Fe(III) at pH 10 is the disappearance of a broad feature around

1365 cm^{-1} assigned to ν(CC) with contributions from the δ(OH). These spectral changes were

interpreted to indicate the formation of monodentate and bidentate mononuclear pyrocatechol-Fe

complexes under acidic and basic conditions, respectively. Given the close resemblance between

the spectra of fully protonated pyrocatechol and the one with Fe(III) present, the latter spectrum

could also be assigned to a mixture of uncomplexed fully protonated pyrocatechol and a

mononuclear bidentate pyrocatechol-Fe complexe. This latter interpretation is supported by the

relatively small complexation constant of pyrocatechol-Fe complex ([Fe(cat)]$^+$), K_c = (4.35 ±

0.1) × 10^{-2} at 25°C in the pH range 1-2.[51] The aforementioned spectral analysis of organics in the

aqueous phase and their complexes with soluble Fe(III) will provide key insights into similarities

and differences in their complexation mechanism to hematite nanoparticles presented in the

following section.

(B) Spectral characterization of surface organics as a function of pH

The left panel of Fig. 2 shows ATR-FTIR absorbance spectra of adsorbed citrate, oxalate

and pyrocatechol on hematite nanoparticles as a function of decreasing pH in the range 9-5.

Similar spectra were collected as a function of decreasing pD for solutions prepared in liquid

D_2O as shown in Fig. S7. The spectral range shown in Fig. 2 contains the band assigned to the

bending mode of water, $\delta(H_2O)$, at 1639 cm^{-1}, which shifts to 1206 cm^{-1} in liquid D_2O.[52] This

feature is subtracted out by spectral referencing to the background spectrum collected prior to

introducing the organic solutions. As mentioned above, the spectral range shown contains

$\nu(CO_2^-)$ and $\nu(CO)$ sensitive to protonation and binding to metal oxides. This spectral range

also contains absorptions due to surface carbonate given that our experiments were conducted in

air. In order to investigate the degree of carbonate interference with the spectra shown in Fig. 2,

control experiments were conducted where background and organic solutions were purged with

N_2 gas before and during the flow of solutions over the hematite nanoparticles film. Comparison

spectra with air are shown in Fig. S8 and compared to a control spectrum collected after flowing

a sodium hydrogen carbonate solution over a similar film. The peaks at 1497, 1342 and 1068

cm^{-1} are assigned to surface carbonate, which are spectrally shifted relative to those assigned to
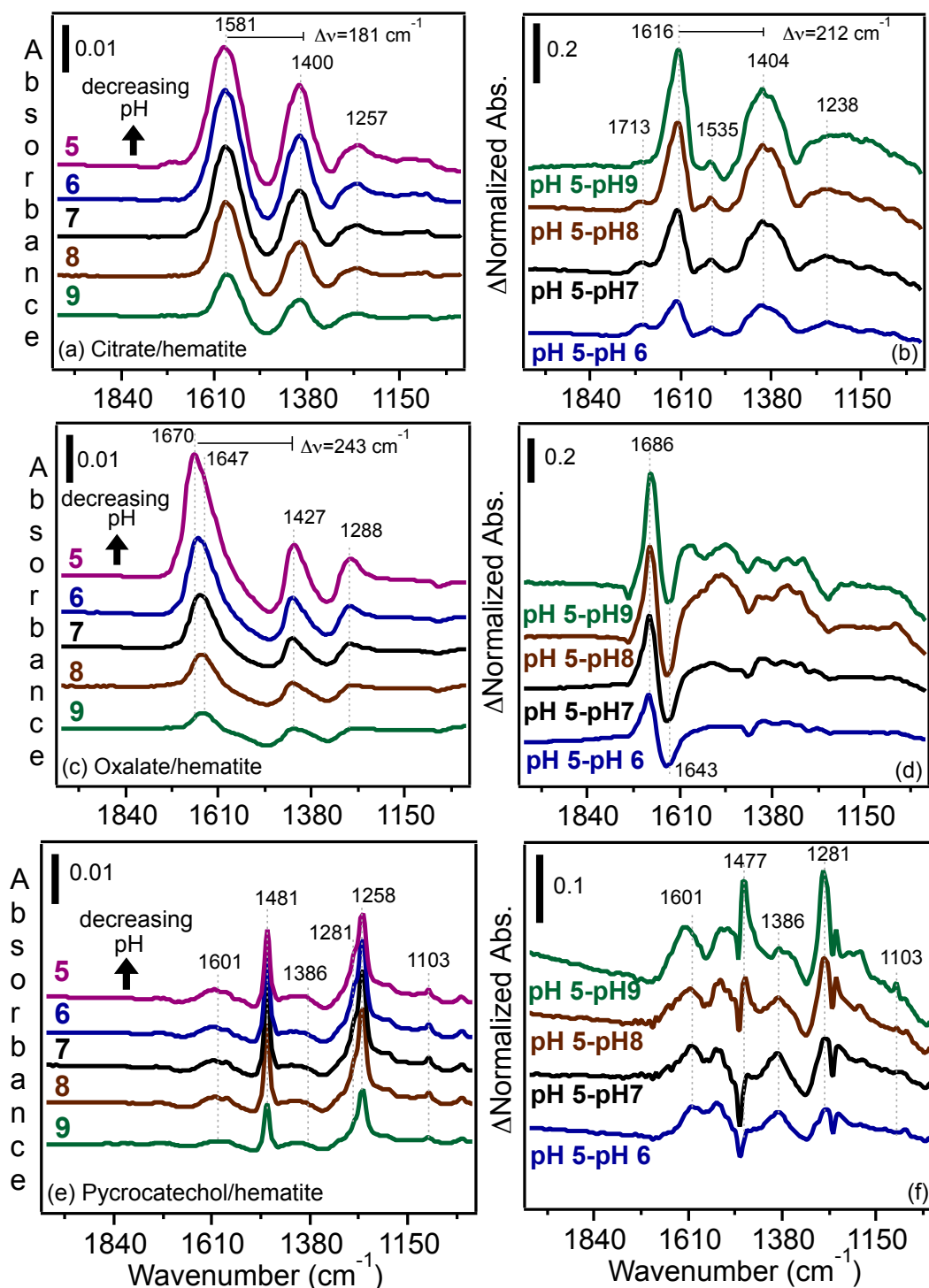
Fig. 2: Representative ATR-FTIR absorbance and difference spectra of adsorbed (a,b) citrate, (c,d) oxalate, and (e,f) pyrocatechol on hematite nanoparticles after flowing 10^{-4} M aqueous solutions for 30 min as a function of decreasing pH from 9 to 5. The electrolyte concentration was 0.01 M KCl, which is 100x higher than [organics(aq)]. The procedure for obtaining the difference spectra shown in the right panel is described in the text.

surface citrate, oxalate and pyrocatechol. Based on this data, we concluded that surface

carbonate has minimum interference with the peaks assigned to surface organics studied herein.

The spectra in Fig. 2 were collected *in situ* while flowing the respective organic solutions (10^{-4} M

and 10 mM KCl) for 30 min over the surface. Longer equilibrium time up to 80 min did not

cause a significant increase in absorbance assigned to the adsorbed organics, and hence, an

equilibrium time of 30 min was deemed sufficient. These spectra were used to elucidate the

structure of surface complexes, taking into account the IEP of hematite nanoparticles at 8.45, the

aqueous phase speciation of the organics shown in Fig. S4, and their signature IR absorbances as

assigned in Table 1.

At pH 9, the hematite nanoparticles surface is negatively charged due to the high

concentration of $\equiv$FeO$^-$ sites. Also, at this pH, the fully deprotonated species of citric acid, CA^{3-},

is the most dominate species. Decreasing the pH below the IEP increases the concentration of

$\equiv$FeOH and $\equiv$FeOH$_2^+$ sites, and therefore increases the favorability of ligand exchange driven by

electrostatics.   Despite unfavorable electrostatic repulsion under basic conditions, citrate

adsorption takes place at this basic pH giving rise to peaks at 1581, 1400 and 1257 cm^{-1}, which

do not shift in frequency with decreasing pH (Fig. 2a). The value of $\Delta\nu$ among the $\nu(CO_2)$

features is 181 cm^{-1}, which is in between the 193 and 178 cm^{-1} calculated for aqueous phase

complexed and free citrate species, respectively, in Fig. 1 (right). Decreasing the pH to 5

increases the concentration of protonated aqueous phase HCA^{2-} and H_2CA^- species, and also

might lead to protonation of adsorbed citrate. The possibility for partial protonation of the

monodentate citrate complexes is similar to that observed for surface carbonate[53,54], phosphate[55,56]

an sulfate[57,58] on hematite and goethite. When spectra in Fig. 2a is compared to those in Fig. S7a

that highlight the effect of the H/D exchange, little spectral shift is observed for the intense

features at 1581 and 1400 cm^{-1}. The weak feature at 1257 is blue-shifted to 1280 cm^{-1}, suggesting strong hydration influence on this mode, which is assigned to $\delta(CO_2^-)$ in Table 1.

To further examine changes in surface speciation of adsorbed citrate with decreasing pH, all spectra were normalized to the absorbance at 1581 cm^{-1}, and then subtracted from that collected at pH 5. These difference spectra are shown in Fig. 2b with clear positive features at 1713, 1616, 1535, 1404 and 1238 cm^{-1}. Upon comparing these infrared frequencies with those of aqueous phase citric acid and soluble iron(III) citrate complexes listed in Table 1, it becomes clear that the frequencies at 1616 and 1535 cm^{-1} are new. The former is assigned to $\nu(COFe)$ in inner-sphere complexes given its proximity to the frequencies observed for soluble iron(III) citrate complexes in Table 1 and Fig. S5. The latter peak at 1535 cm^{-1} is red-shifted by *ca*. 40 cm^{-1} from $\nu_a(CO_2^-)$ in bulk phase spectra, and hence is assigned to free and uncomplexed $\nu(CO_2^-)$ moiety *in the* inner-sphere citrate complex. This feature could also arise from outer-sphere citrate complexes based on the earlier conclusions by Yeasmin *et al*.[23] and Chernyshova *et al*.[26] Because of the relatively low intensity of this feature relative to the $\nu_s(CO_2^-)$ at 1404 cm^{-1}, it is likely that outer-sphere complexes exist at a lower concentration than inner-sphere complexes. This conclusion was also inferred from electrolyte concentration-dependent adsorption studies and desorption by variable concentrations of Cl$^-$ (aq) described below. The spectral feature at 1713 cm^{-1} (Fig. 2b) is red shifted relative to the 1722 cm^{-1} in fully protonated and singly deprotonated citric acid species at pH 2 and 4 (Fig. 1, left), and can be explained in two ways: (1) the formation of citrate inner-sphere complexes is favored under acidic conditions leading to strengthening the carbonyl character in the complexed citrate due to COFe groups, or (2) the enhancement in the intensity of the 1713 cm^{-1} feature under acidic conditions along with the weak feature around 1238 cm^{-1} assigned to $\nu(COH)$ is an indirect evidence of protontation of

uncomplexed $-CO_2^-$ moieties in either inner- or outer-sphere surface citrate. Based on this analysis, a pictorial representation of citrate surface complexes on hematite nanoparticles with decreasing pH is shown in Scheme 1a.
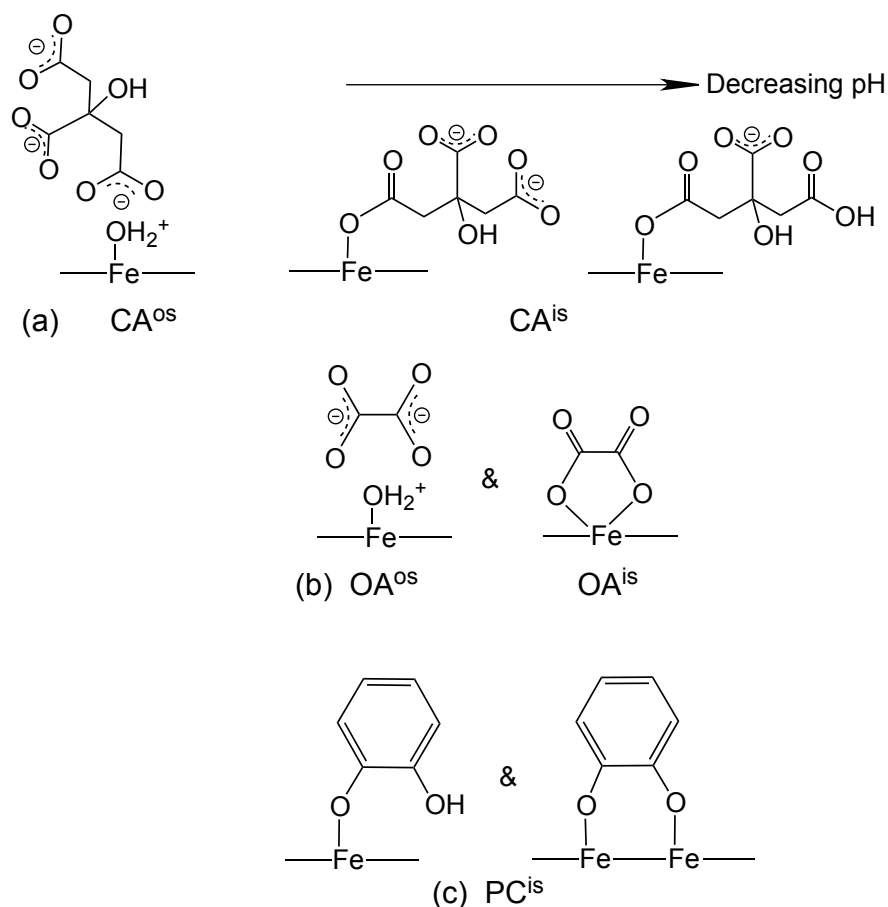
Scheme 1: Structures of surface complexes as inferred from pH- and electrolyte concentration-dependent infrared spectroscopic studies. Solvent molecules and electrolyte ions were removed for clarity. The arrow shows the direction of decreasing pH and the corresponding surface complexes under acidic (right) versus basic (left) conditions.

Fig. 2c shows ATR-FTIR absorbance spectra of surface oxalate (OA) with decreasing pH and the assignment of the peaks is listed in Table 1 based on the discussion below. Per the speciation curve of oxalic acid shown in Fig. S4b, the most dominant aqueous phase species is

OA^{2-} in the pH range 9-5 with less than 10% HOA$^-$ at pH 5. The spectra of adsorbed oxalate at pH 9 and 8 show a feature at 1647 cm^{-1} which blue shifts to 1670 cm^{-1} at pH 5. This is accompanied by an increase in the intensity of features at 1427 and 1288 cm^{-1}. The value of $\Delta\nu$ among the $\nu(CO_2)$ features increases from 220 to 243 cm^{-1} with decreasing pH (Fig. 2c). This 23 cm^{-1} increase follows the trend in $\Delta(\Delta\nu)$ shown in Fig. 1 (left) between free and complexed aqueous phase oxalate, where the difference is 22 cm^{-1}. Based on this analysis, the data suggests changes in the type of oxalate complexes with decreasing pH. When spectra in Fig. 2c is compared to those in Fig. S7b that highlight the effect of the H/D exchange, shifts are observed for the most intense feature to 1655 and 1662 cm^{-1} with decreasing pD. This feature has relatively narrower width than those in Fig. 2c and $\Delta\nu$ of 235 cm^{-1}. This suggests strong hydration influence on this mode due to outer-sphere complex formation as detailed below.

To isolate the new spectral components responsible for the blue shift in the 1647 cm^{-1} peak (Fig. 2c), normalized spectra collected at 6, 7, 8 and 9 were subtracted from that at pH 5 as shown in Fig. 2d. This subtraction procedure clearly shows the growth in a component at 1686 cm^{-1} that is most pronounced between acidic and basic conditions and a loss feature at 1643 cm^{-1}. The former feature indicates strengthening of the carbonyl character in surface oxalate, and the loss feature is assigned to the bending mode of surface water. These difference spectra suggest ligand exchange with surface water under acidic conditions enhancing the formation of inner-sphere oxalate with stronger and uncomplexed C-O bonds than under basic conditions.

Previous studies have concluded that over the pH range 9-5, oxalate adsorption is dominated by outer-sphere complexation.[17,33] The interpretation in these studies relied on comparing the spectra of adsorbed oxalate with those from the aqueous phase species with no Fe(III) present. However, spectra shown in Fig. 1 (right) for aqueous phase oxalate at pH 7 does

not resemble those collected for adsorbed oxalate in Fig. 2c. A better indicator for comparison would be the shifts in $\Delta\nu$ among aqueous phase oxalate (free and complexed) and those of surface oxalate (see above). Based on this criterion, the data suggest that outer- and inner-sphere complexes of oxalate are dominant under basic and acidic conditions, respectively. The spectral feature characteristic of outer-sphere complexation is the one at 1647 cm^{-1} (shifts to 1655 cm^{-1} in D$_2$O, Fig. S7b). The uncomplexed -CO$_2^-$ moieties in the outer-sphere complexes will be in conjugation and hence have less carbonyl character. Inner-sphere complexation forming stable five-membered ring surface oxalate[33] strengthens the uncomplexed C-O bonds giving rise to components at 1686 cm^{-1} (Fig. 2d). However, due to the co-existence of outer-sphere complexes and that IR spectroscopy shows the sum of adjacent peaks, the IR signature of inner-sphere complexes appears at 1670 and 1662 cm^{-1} under acidic conditions (Fig. 2c and S7b). Based on this analysis, a pictorial representation of oxalate surface complexes on hematite nanoparticles with decreasing pH is shown in Scheme 1b. As described in detail below, the effect of electrolyte concentration on the adsorption and the desorption behavior of surface organics gives a better indication of the relative amounts of weakly- versus strongly-bonded complexes than mere comparisons with bulk aqueous phase spectra.

The spectra shown for adsorbed pyrocatechol (PC) in Fig. 2e were analyzed in a similar fashion as for adsorbed citrate and oxalate. Over the pH range 9-5, the chemical species of pyrocatechol in the aqueous phase are a mixture of the singly deprotonated HPC$^-$ and fully protonated H$_2$PC under basic conditions, and dominated by the H$_2$PC species under neutral to acidic conditions (Fig. S4c). Despite the unfavorable repulsion with negative surface sites under basic conditions, adsorption of pyrocatechol does take place giving rise to intense features at 1481 and 1258 cm^{-1} with a shoulder around 1281 cm^{-1}. This data suggests inner-sphere

complexation, and hence the aforementioned spectral features are assigned to ν(COFe). The spectra in Fig. 2e and Fig. S7c show little shifts with decreasing pH and pD and when using D_2O as a solvent, respectively. However, the results of the spectral subtraction in Fig. 2f show the growth of features at 1601, 1477, 1386 and 1281 cm^{-1} and a loss in the component at 1489 cm^{-1} under acidic conditions. When comparing these frequency values to those assigned to aqueous phase pyrocatechol and its soluble complexes with Fe(III) in Table 1, the spectral features in Fig. 2e can be assigned to mostly bidentate inner-sphere complexes with increasing concentration of protonated monodentate inner-sphere complexes with decreasing pH characterized by the features at 1601 and 1281 cm^{-1}. The latter features are the most sensitive to H/D exchange as their intensity diminishes considerably when using D_2O as a solvent (Fig. S7c). The co-existence of both types of surface complexes has been observed previously on the surface of goethite particles, where it was inferred that the bidentate surface complex is binuclear instead of mononuclear.[25] As described below, this interpretation is further supported with adsorption and desorption experiments performed herein as a function of electrolyte concentration, where [KCl(aq)] is 10-1000x higher than [organic(aq)].

Fig. 3 shows the dependency of the amount of adsorbed organics on [KCl(aq)] in the range 10^{-3} – 1000 mM at pH 7. Also shown for comparison the amount adsorbed of citrate and oxalate using 1000 mM KBr and NaCl. These experiments were conducted using 1 mM of each organic compound, which is near surface saturation per the adsorption isotherms shown in section C below. The y-axis represents the normalized corrected absorbance at 1581, 1667, and 1258 cm^{-1} to the values at 1000 mM KCl. These frequencies are characteristic of the corresponding surface complexes at pH 7, whose intensity is proportional to surface coverage. The normalization process cancels out the contribution of molar absorptivity of each vibrational
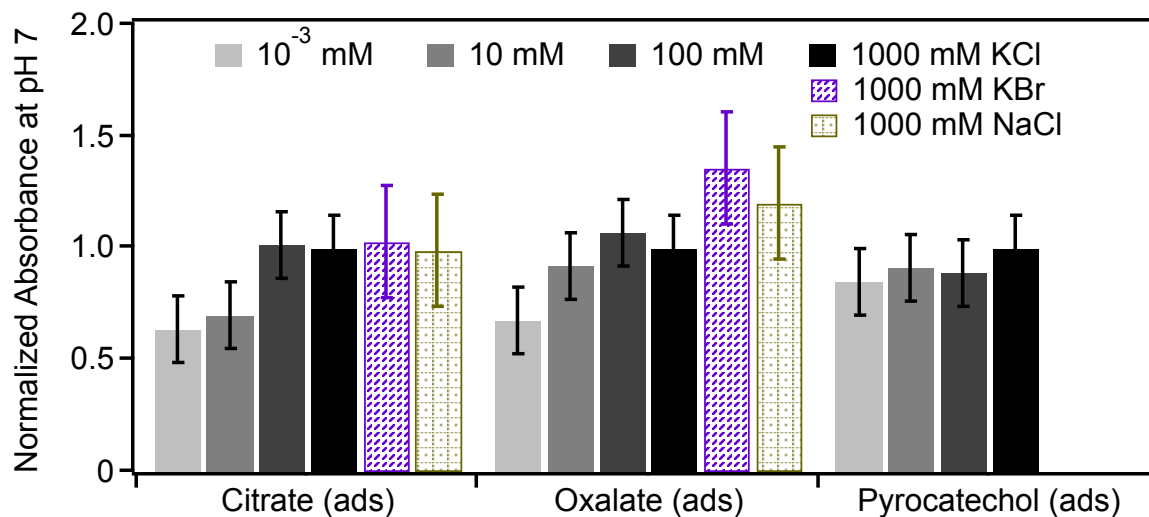
Fig. 3: Effect of electrolyte concentration on the amount adsorbed of citrate, oxalate and pyrocatechol on hematite nanoparticles at pH 7 after flowing 1 mM of each organic solution for 30 min. Electrolyte concentration was adjusted using KCl, KBr and NaCl.

mode, allowing for comparisons among three organic compounds. For surface citrate, there is a 40% increase in the amount adsorbed upon increasing electrolyte concentration to 100 and 1000 mM. This trend on hematite nanoparticles is different than that reported on goethite as discussed in the introduction[30] and can be explained by the effect of electrolyte concentration on the thickness of the double layer, which decreases with increasing electrolyte concentration.[43] At *low electrolyte concentration using only 1 mM [organic(aq)]*, the double layer is thick and spectroscopic analysis used herein can detect electrostatic adsorption to a certain extent. Increasing electrolyte concentration at pH 7 will result in altering surface charge.[43]

The molecular-level picture of electrolytes interactions with hematite colloids in aqueous solutions was investigated in a series of studies using cryogenic x-ray photoelectron spectroscopy (XPS).[59-61] Also, these interactions were theoretically predicted using molecular dynamics (MD) simulations at a *neutral* (100) goethite surface.[62] Surface loadings of anions and cations from XPS-derived data from *frozen* hematite pastes previously equilibrated in 50 mM

electrolyte solutions (pH 2– 11) showed these trends: $F^- > I^- \approx Cl^- > Br^-$ and Na(F) > Na(I) > Na(Br) > Na(Cl).[61] The MD calculations at 300 K with NaCl, CsCl and CsF revealed the presence of a structured interfacial region resulting from the strong interaction of water with the goethite surface.[62] A buildup of positive charges near the surface was found as a result of cations adsorption leading to accumulation of anions in the next few angstroms. These MD calculations predict the presence of several condensed layers and oscillations in the net charge away from the surface. For comparison with deliquesced salt surfaces, XPS experiments and MD predictions at room temperature show enhancement of Br^- and I^- near the interface compared with Cl^- and F^-.[63] Comparing our measurements at room temperature with continuous flow of background solution to XPS data using frozen hematite paste samples is not straight forward given the effect of temperature and hydration conditions on the thermodynamics and kinetics of adsorption.[64] Still, these XPS and MD results and those on salt solutions can aid in explaining the trend in Fig. 3 for increasing amount of surface citrate with increasing electrolyte concentration: the hematite surface is positively charged at pH 7, increasing concentrations of $Cl^-(aq)$ and $K^+(aq)$ will result in aligning the negative charges near the surface and positive charges further from the surface. Hence, incoming HCA^{2-}/CA^{3-} molecules experience a much greater degree of electrostatic attraction at higher electrolyte concentration leading to more adsorption. The data in Fig. 3 for citrate shows little effect of the $Br^-(aq)$ and $Na^+(aq)$ on the amount adsorbed at pH 7 after 30 min flow for the highest electrolyte concentration. This is likely because in both cases, the incoming HCA^{2-}/CA^{3-} molecules 'see' the positive charges from either $K^+(aq)$ or $Na^+(aq)$ irrespective of the underlying anion, and –as explained below- citrate adsorption is dominated by inner-sphere compelxation.

In an effort to determine the type of surface citrate complexes with increasing electrolyte concentration, Fig. S9a shows representative difference spectra obtained by subtracting those collected at lower [KCl(aq)] from those at higher [KCl(aq)]. There is a clear enhancement in spectral components at 1558, 1454 and 1365 cm^{-1} with $\Delta\nu = 193$ cm^{-1} most pronounced in the difference spectra of the highest and lowest electrolyte concentration. This value of $\Delta\nu$ is identical to that calculated from the spectra of complexed citrate in *the bulk aqueous phase* shown in Fig. 1 (right). The absence of $\nu(C=O)$ around 1720 cm^{-1} from the spectra in Fig. S9a rules out monodentate mononuclear citrate complexes. Also, the components in Fig, S9a appear at frequency values far from those observed in Fig. 1(right) for complexed citrate in the aqueous phase. The most likely conclusion based on the above is that the peaks at 1558, 1454 and 1365 cm^{-1} originate from outer-sphere citrate complexes with conjugated C-O bonds stabilized by electrolyte ions at the interface at pH 7. It is important to emphasize here that comparisons between difference spectra shown in Fig. 2b and S9a can not be made because the former shows changes in surface speciation using 0.01 M KCl with decreasing pH, whereas the latter shows changes at pH 7 with increasing [KCl(aq)].

This assignment to the existence of outer-sphere citrate complexes at pH 7 is further supported with desorption data shown in Fig. 4, which shows 2x increase in the amount desorbed by Cl$^-$(aq) relative to the control case (10^{-3} mM). Within the uncertainty of the measurements, further increase in the [Cl$^-$(aq)] does not remove additional citrate suggesting retention of strongly-bonded inner-sphere complexes after 80 min of flowing desorbing agents. Fig. 4 also shows that using 1000 mM Br$^-$(aq) as a desorbing agent has the same effect as Cl$^-$(aq) at the same concentration, even with Na$^+$(aq) as the counter cation. To extract the spectral features of residual citrate after 80 min flow of Cl$^-$ (aq) and Br$^-$ (aq), Fig. S10a show difference spectra
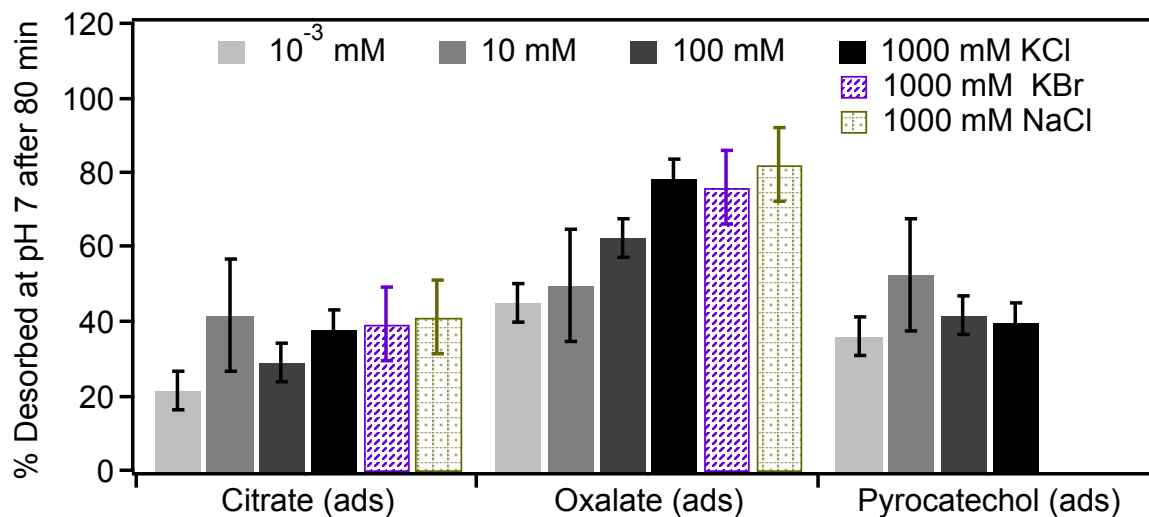
Fig. 4: Percentage desorbed of surface citric acid, oxalic acid and pyrocatechol from hematite nanoparticles after flowing KCl(aq), KBr(aq) and NaCl(aq) for 80 min at pH 7.

relative to the surface prior to flowing the desorbing agents. There are two positive features at 1620 cm^{-1} (KCl), 1616 cm^{-1} (KBr) and 1420 cm^{-1}, which are absent from the features observed in the difference spectra as a function of electrolyte concentration (Fig. S9a). This results confirms the assignment of the aforementioned frequencies to inner-sphere citrate complexes. Also, the high frequency features in Fig.S10a are very close to the 1616 cm^{-1} feature in Fig. 2b under acidic conditions that favor inner-sphere formation. Hence, the desorption process at pH 7 by halide ions removes weak outer-sphere complexes leaving behind strongly-bonded inner-sphere complexes. Scheme 2a shows a pictorial representation of the surface and the diffuse layers highlighting the role of electrolytes in citrate adsorption.

The trends for oxalate adsorption as a function of electrolyte concentration in Fig. 3 show that adding electrolytes as low as 10 mM would increase the amount adsorbed by 35±10%. Further increase in electrolyte concentration does not result in any appreciable effect when accounting for the uncertainty in the experimental data. At first glance, this indicates that at pH 7, inner-sphere oxalate dominates outer-sphere complexes. Indeed, difference spectra in Fig. S9b
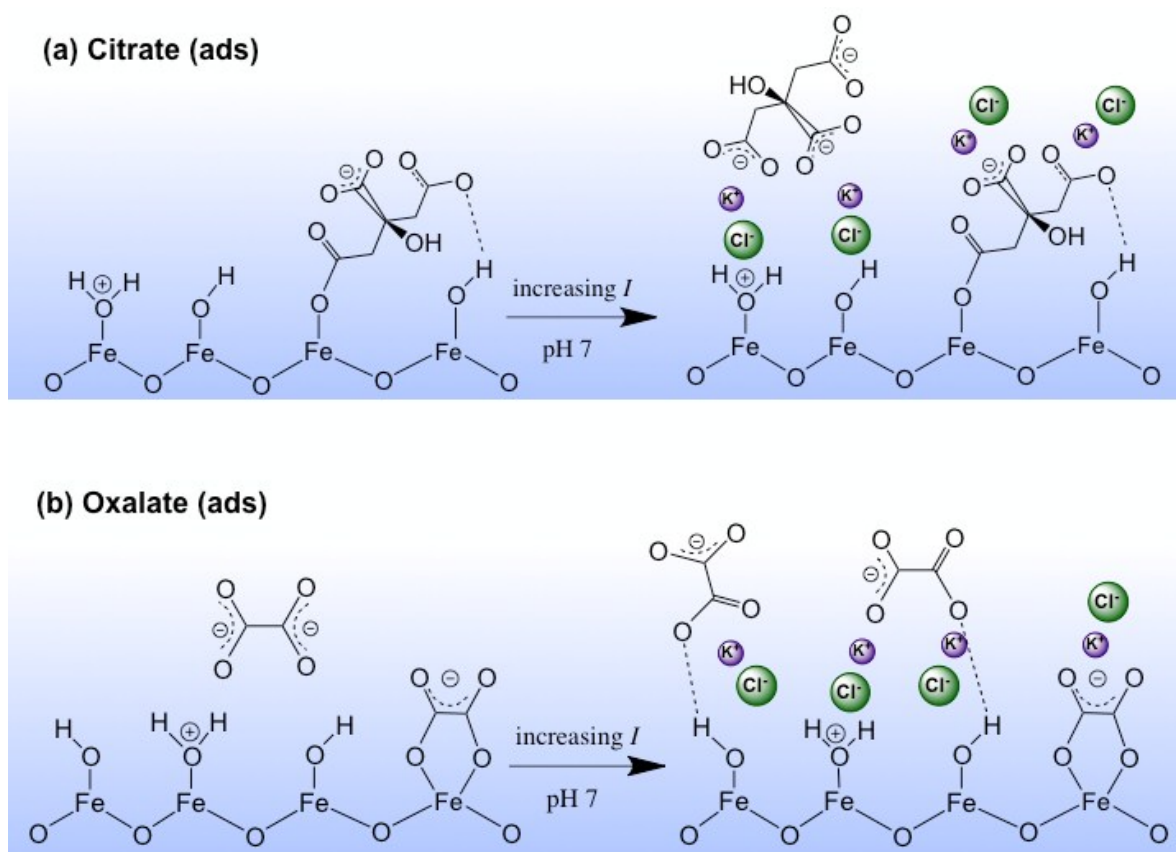
Scheme 2: Effect of increasing I (through varying [KCl(aq)]) on the surface speciation of (a) citrate, and (b) oxalate on hematite nanoparticles at pH 7.

show the growth in a spectral component at 1686 cm^{-1} assigned above to inner-sphere oxalate.

Yet, the trend in the %desorbed of oxalate shown in Fig. 4 tells a different story, where flowing

Cl$^-$ (aq) (from either KCl or NaCl) in concentrations as low as 10^{-3} mM causes nearly 50% of the

surface species to desorb, which increases to 52, 65 and 80% with 10, 100 and 1000 mM over 80

min flow time. Also, about 80% of surface oxalate desorbs using 1000 mM Br$^-$(aq) as a

desorbing agent. It is unlikely that at *pH 7* and over the longest equilibrium time used in our

experiments (100 min) that oxalate-promoted dissolution took place, or that an inner-sphere

mononuclear bidentate oxalate complex will desorb readily as observed. The more plausible

explanation is based on the role that layering of interfacial electrolyte ions plays in affecting electrostatic adsorption as explained above: buildup of positive charge through K^+(aq) at the interface stabilizes oxalate surface complexes, and enhances the formation of hydrogen bonds with the surface. This leads to strengthening C-O bonds explaining the intensity increase at 1686 cm^{-1} in Fig. S9b. Using 1000 mM KBr and NaCl cause a slight enhancement in the amount of adsorbed oxalate after accounting for the uncertainty in the data relative to 1000 mM KCl, with Br^- (aq) having a higher effect. As discussed above for results from XPS and MD calculations, the enhancement in Br^-(aq) near the interface likely leads to increased concentration of positive charge more than Cl^-(aq) leading to more outer-sphere oxalate complexation. This effect was not as pronounced for citrate adsorption because it is dominated by inner-sphere complexation. To extract the spectral features of residual oxalate after 80 min flow of Cl^- (aq) and Br^- (aq), Fig. S10b shows difference spectra relative to the surface prior to flowing the desorbing agents. There are only negative features at 1686, 1531 and 1311 cm^{-1}, suggesting no oxalate was retained by the hematite nanoparticles under these conditions. Further evidence for the dominance of outer-sphere complexation for oxalate is provided below from H/D exchange experiments. Scheme 2b shows a pictorial representation of the surface and the diffuse layer highlighting the role of electrolytes in enhancing oxalate complexation and the dominance of outer-sphere complexes.

For comparison, the effect of electrolyte concentration on oxalate adsorption on goethite was reported by Mesuere and Fish[34] from *ex-situ* batch experiments, where a 22% reduction in adsorbed oxalate was reported using 500 mM KNO_3 relative to 10 mM. This observation was explained by the relatively weak intrinsic affinity of oxalate to goethite, and hence its sensitivity to the decrease in positive potential in the plane of adsorption. This contrast with our results can

be attributed to differences in experimental procedures and type of material. In batch

experiments, the organic solution in equilibrium with the surface is removed so that analysis of

the amount adsorbed could be done. This step will favor inner-sphere over weaker outer-sphere

complexes. For example, Myneni *et al.*[65] showed with an example oxyanion, arsenate, that

changes in the hydration conditions of the surface result in changing the geometry of weakly

adsorbed surface-bound species. Also, goethite has different surface potential and activity than

hematite. Hence, trends as a function of electrolyte concentration reported from these studies

have major contributions from inner-sphere rather than outer-sphere complexes, whereas in our

in situ flow mode experiments, the organic solution is at equilibrium with the surface during the

measurements of surface species. Hence, data reported herein is sensitive to contributions from

both types of surface complexes. Also, given that interfacial layering of electrolyte ions were

highlighted to be important from modeling studies[62] and experimental studies[59-61], they can not be

ruled out from enhancing outer-sphere complexation as observed herein.

Fig. 3 shows that there is little effect of increasing electrolyte concentration on the

%adsorbed of pyrocatechol using a solution concentration that will result in about 80% surface

saturation at pH 7 (see below). A similar effect was reported earlier by Bullen and co-workers.[24]

Flowing variable concentrations of Cl⁻ (aq) in desorption experiments results in about 40%

amount desorbed, and hence over 60% being retained on the surface. This is in line with the

interpretation of infrared spectra above where it was inferred that pyrocatechol forms a mix of

mono- and binuclear bidentate inner-sphere surface complexes. The desorption experiments

highlight the relative amounts of each type, where it could be concluded that at pH 7, the

majority of pyrocatechol forms the latter type. This combination of adsorption and desorption

studies under the same experimental settings addresses the difficulty in discerning mono- versus

binuclear bidendate complexes of pyrocatechol from infrared spectroscopy data.[24,66] In contrast

to negatively charged citrate and oxalate surface complexes, the benzene ring of pyrocatechol

will turn the hematite nanoparticles surface into a hydrophobic one, changing by that the

structure of interfacial water, interactions with electrolytes, and affinity to charged, polar and

nonpolar compounds. In the following section, binding thermodynamics of surface complexes

are provided as elucidated from the spectral interpretation detailed above.

(C) Thermodynamic analysis using the triple layer SCM from adsorption isotherms and pH envelopes.

The triple layer model was fit to the adsorption pH envelope and isotherm data at pH 7 of

citrate, oxalate, and pyrocatechol on hematite nanoparticles, both as one combined data set and

as isotherm and envelope data individually (Fig. 5). Consistent with spectroscopic results

described in the previous section, the triple layer SCM was able to describe citrate adsorption

with one protonated inner-sphere complex with one negative charge, and one deprotonated outer-

sphere complex with net 2 negative charges as shown in reactions 1 and 2. The best fit

parameters are listed in Table 2 along with the quality of the fit, as measured by the overall

variance V_y = SOS/DF, where SOS is the weighted sum of squares of the residuals and DF is the

degrees of freedom. The smaller the value of V_y, the closer the fit of the model to the

experimental data. Not surprisingly, the fit for the combined data set was of relatively lower

quality than that for isotherms and envelopes fit individually. Also listed in Table 2 are

calculated values of the free energy of adsorption, ΔG°_{ads}, to better highlight differences in

thermodynamic favorability for the formation of different types of surface complexes. For the

citrate adsorption data (Figs. 5 a,d), there is an excellent agreement between the model with two
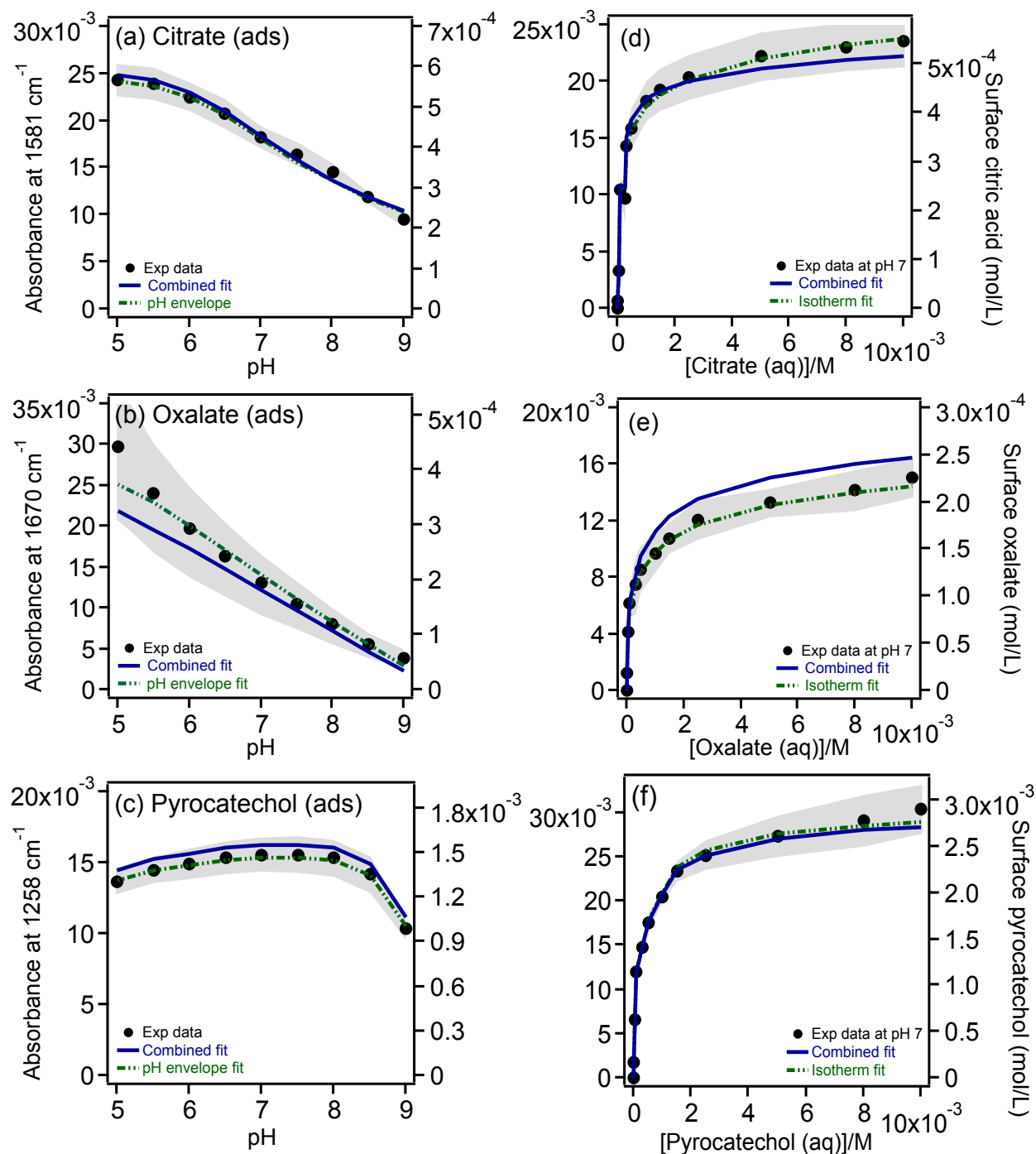
Fig. 5: Experimental data (solid markers) and SCM fits (lines) for the adsorption of citrate, oxalate and pyrocatechol on hematite nanoparticles as a function of pH (a-c) and concentration (d-f) at pH 7. The electrolyte concentration is 10 mM KCl. Best fit parameters are listed in Table 2. The shaded area represents the standard deviation in absorbance from averaging 4-6 experiments.

Table 2: Tripe layer SCM constants from the individual and combined model fits to the pH envelope and adsorption isotherm experimental data at pH 7

Compound	Type of Surface Complexes	Fitting pH Envelopes		Fitting Adsorption Isotherm at pH 7		Fitting isotherm and envelope simultaneously	
		LogK (ΔG°_{ads} / kJ/mol)	Vy	LogK (ΔG°_{ads} / kJ/mol)	Vy	LogK (ΔG°_{ads} / kJ/mol)	Vy
Citrate	Protonated inner-sphere with 1 negative charge	5.03 (-28.7)	9.4	5.71 (-32.6)	3.2	5.28 (-30.1)	10.3
	Deprotonated outer-sphere with *net* 2 negative charges	2.70 (-5.5)[a]		1.2 (+3.1)[a]		2.75 (-5.7)[a]	
Oxalate	Doubly deprotonated outer-sphere with inaccessible neighboring site	10.55 (-60.2)	38.9	10.08 (-57.5)	0.9	10.48 (-59.8)	87.6
	Deprotonated inner-sphere	6.74 (-38.5)		5.61 (-32)		6.09 (-34.7)	
Pyrocatechol	Inner-sphere bidentate binuclear	6.16 (-55.1)[b]	0.6	7.03 (-60)[b]	3.4	6.85 (-59)[b]	9.1

Notes: [a] Because K^1_{CA} in eq.(7) has net units of M, $\Delta G^{\circ}_{ads} = -RT\ln\left[K(M)/55.5M\right]$, where 55.5 M is the concentration of water, and T = 298 K. [b] Because K_{PC} in eq.(10) has net units of M^{-2}, $\Delta G^{\circ}_{ads} = -RT\ln\left[K(M^{-2}) \times (55.5M)^2\right]$.

different types of surface complexes and experimental data, with the inner-sphere complex being more thermodynamically favorable. The inner- and the outer-sphere surface complexes are present in approximately comparable concentrations at pH 7. This relative concentration changes with pH, and the concentration of the outer-sphere complex always dominates. However, above pH 8 the inner-sphere surface complexes are present in only trace amounts.

The triple layer SCM model was also able to describe oxalate adsorption using one

doubly-deprotonated outer-sphere surface complex with an inaccessible neighboring site, and one inner-sphere mononuclear bidentate surface complex as shown in reactions 2 and 3. The model fits the isotherm data very well within the uncertainty of the experimental measurements. There is also excellent agreement with the pH envelope data in the range 9-5.5. The combined fit does deviate from experimental data below pH 6, because of incorporating surface complexes dominant at pH 7 from the isotherm measurements. The formation of the outer-sphere surface complex is more thermodynamically favorable, and it constitutes about two-thirds the relative concentration of the inner-sphere surface complex at pH 7. The inner-sphere surface complex becomes dominant above pH 8 (i.e., basic conditions). Also, as discussed in the above sections, the inner-sphere oxalate complex is important in enhancing the dissolution of iron-(oxhydr)oxides under very acidic conditions, pH < 3, and over hours to days of equilibrium time.[67] The pH range studied herein and equilibrium time during experiments do not drive the formation of inner-sphere oxalate in large concentrations that affects dissolution rate of hematite nanoparticles.

Moreover, Figs. 5c and 5f show the adsorption pH envelope and isotherm data of pyrocatechol along with the fitting results using reaction 5 for one inner-sphere binuclear bidentate complex. Best fit parameters are listed in Table 2. Attempts to add a second reaction to the mechanism to describe inner-sphere monodentate surface complex formation were made, once by adding reaction 11, and once by adding reaction 12:

$$FeOH + H_2PC \leftrightharpoons FeHPC + H_2O \tag{11}$$

$$2FeOH + H_2PC \leftrightharpoons FeOHFeHPC + H_2O \tag{12}$$
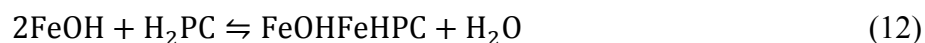
The triple layer SCM converged with reaction 11 only, but the SOS/DF for the isotherm, pH and combined fits were larger than using reaction 5 only. This model did not converge when fitting

the pH envelope and isotherm data using both reactions 5 and 11. Reaction 12 is identical to reaction 5 because the triple layer SCM does not take into account water molecules. The excellent agreement between the model results and experimental data shown in Figs. 5c and 5f can be interpreted to indicate the dominance of the binuclear bidentate inner-sphere complex over the pH range studied herein.

In summary, the triple layer SCMs described above from the *in situ* spectral data of organics adsorption on hematite nanoparticles provide mechanism-based thermodynamic models and parameters that could be used for future predictions of the surface chemistry of that interface. Also, the results reported herein would be applicable to hematite nanoparticles in the same particle size and shape. Larger particles with the same shape would decrease the surface area and that will lead to lower intensities of peaks assigned to surface organics. On the other hand, smaller particles of the same shape would result in an increase in surface area and hence increasing intensities of peaks assigned to surface organics. However, if smaller hematite particles have different and non-spherical shapes, they will expose different defects and surface planes[68,69] that might give rise to different types of surface organic complexes, which in turn would manifest themselves through shifts in ν(CO) distinguishable from those observed with spherical particles.

Conclusions

Spectroscopic data are reported herein for the adsorption pH envelopes and isotherms at pH 7 using ATR-FTIR for citrate, oxalate and pyrocatechol on hematite nanoparticles. The spectroscopic experiments were coupled with the application of the triple layer SCM derived for each organic compound based on the interpretation of spectral data. Results indicate that the

structure of the organic species affects the type of surface complexes formed with consequences on surface charge as shown from electrolyte concentration-dependent studies. In the case of citrate and oxalate adsorption, the positively-charged surface switches to negatively-charged at pH values below PZC (recorded in the absence of organics). The extent of outer-sphere complexation of these two organics was sensitive to adjustments in electrolyte concentration causing an overall enhancement in the amount adsorbed with increasing electrolyte concentration. Also, compared to oxalate, hematite nanoparticles retain more citrate and pyrocatechol when flowing Cl^-(aq) at pH 7. Under the experimental conditions described herein, no effect for changing the cation to Na^+(aq) or the anion to Br^-(aq) was observed on the amount of adsorbed citrate, whereas for oxalate, the enhancement of interfacial Br^-(aq) caused an increase in the amount of adsorbed oxalate due to concentrating more cations near the interface than in the case of Cl^-(aq). This observation and results from H/D exchange experiments supported the spectral analysis that suggests higher amounts of outer-sphere complexation for oxalate than citrate, which is dominated by inner-sphere monodentate complexes. As for pyrocatechol, adsorption and desorption data suggest dominance of bidentate-binuclear complexes.

　　　These results are significant because they clearly show experimental evidence for the effect of interfacial electrolyte layering on adsorption, particularly for systems containing weakly-bonded outer-sphere complexes, oxalate and citrate. The results also highlight that *in situ flow mode* experiments such as those described above can amplify trends otherwise missed in bulk batch adsorption experiments. Given the ubiquity of organic-metal oxide interfaces in environmental and medical systems, particularly those that utilize nanoparticles, mechanistic details at the molecular level are best elucidated from experimental procedures that mimic real

systems and conditions. To complement the thermodynamic parameters reported herein, a forthcoming publication from our group will report the kinetics of adsorption and desorption of these organic compounds to/from hematite nanoparticles from *in situ flow mode* experiments, and how their surface complexes impact the adsorption kinetics of arsenate and dimethylarsinic acid.

Acknowledgments

Electronic supplementary information (ESI) Available

Figures and tables showing additional spectra and detailed analysis.

References

1   S. M. Louie and J. M. Pettibone, *Environ. Sci. Nano*, 2015, 2, 215-300.

2   I. A. Mudunkotuwa and V. H. Grassian, *Environ. Sci. Nano*, 2015, 2, 429-439.

3   A. Philippe and G. E. Schaummann, *Environ. Sci. Technol.*, 2014, 48, 8946-8962.

4   H. Liu, T. Chen and R. L. Frost, *Chemosphere*, 2014, 103, 1-11.

5   R. K. Cross, C. Tyler and T. S. Galloway, *Environ. Chem.*, 2015, 12, 627-642.

6   A. Figuerola, R. Di Corato, L. Manna and T. Pellegrino, *Pharmacol. Res.*, 2010, 62, 126-143.

7   M. Mahmoudi, S. Sant, B. Wang, S. Laurent and T. Sen, *Adv. Drug Delivery Rev.*, 2011, 63, 24-46.

8   A. K. Gupta and M. Gupta, *Biomaterials*, 2005, 26, 3995-4021.

9   W. W. Tang, G. M. Zeng, J. L. Gong, J. Liang, P. Xu, C. Zhang and B. B. Huang, *Sci. Total Environ.*, 2014, 468-469, 1014-1027.

10   D. K. Hore, D. S. Walker and G. L. Richmond, *J. Am. Chem. Soc.*, 2008, 130, 1800-1801.

11   L. F. Scatena, M. G. Brown and G. L. Richmond, *Science*, 2001, 292, 908-912.

12   A. W. Chasse, T. Ohno, S. R. Higgins, A. Amirbahman, N. Yildirim and T. B. Parr, *Environ. Sci. Technol.*, 2015, 49, 9733-9741.

13   J. Hur and M. A. Schlautman, *J. Colloid Inter. Sci.*, 2003, 264, 313-321.

14   K. Lalonde, A. Mucci, A. Ouellet and Y. Gelinas, *Nature*, 2012, 483, 198-200.

15   K. K. Au, A. C. Penisson, S. L. Yang and C. R. O'Melia, *Geochim. Cosmochim. Acta*, 1999, 63, 2903-2917.

16   P. U. Reichard, R. Kretzschmar and S. M. Kraemer, *Geochem. Cosmochim. Acta*, 2007, 71, 5635-5650.

17   D. M. Cwiertny, G. J. Hunter, J. M. Pettibone, M. M. Scherer and V. H. Grassian, *J. Phys. Chem. C.*, 2009, 113, 2175-2186.

18   H. Chen and V. H. Grassian, *Environ. Sci. Technol.*, 2013, 47, 10312-10321.

19   M. A. Blesa, A. D. Weisz, P. J. Morando, G. E. Salfity and A. E. Regazzoni, *Coor. Chem. Rev.*, 2000, 196, 31-63.

20   J. D. Kubicki, L. M. Schroeter, M. J. Itoh, B. N. Nguyen and S. E. Apitz, *Geochim. Cosmochim. Acta*, 1999, 63, 2709-2725.

21   K. Lackovic, B. B. Johnson, M. J. Angove and J. D. Wells, *J. Coll. Inter. Sci.*, 2003, 267, 49-59.

22   M. Lindergren, J. S. Loring and P. Persson, *Langmuir*, 2009, 25, 10639-10647.

23   S. Yeasmin, B. Singh, R. S. Kookana, M. Farrell, D. L. Sparks and C. T. Johnston, *J. Coll. Inter. Sci.*, 2014, 432, 246-257.

24   H. Gulley-Stahl, P. A. Hogan II, W. L. Schmidt, S. J. Wall, A. Buhrlage and H. A. Bullen, *Environ. Sci. Technol.*, 2010, 44, 4116-4121.

25   Y. Yang, W. Yan and C. Jing, *Langmuir*, 2012, 28, 14588-14597.

26   I. V. Chernyshova, S. Ponnurangam and P. Somasundaran, *Langmuir*, 2011, 27, 10007-10018.

27   C. Chen and D. L. Sparks, *Environ. Chem.*, 2015, 12, 64-73.

28   T. Karlsson and P. Persson, *Chem. Geo.*, 2012, 322-323, 19-27.

29   H. J. Shipley, K. E. Engates and A. M. Guettner, *J. Nanopart. Res.*, 2011, 13, 2387-2397.

30   J. D. Filius, T. Hiemstra and W. H. Van Riemsdijk, *J. Coll. Inter. Sci.*, 1997, 195, 368-380.

31 W. Stumm, in *Aquatic Chemistry-interfacial and interspecies processes*, eds. C. P. Huang, C. R. OMelia and J. J. Morgan, ACS, Washington DC, 1995, vol. 244, pp. 1-32.

32 W. Stumm, *Chemistry of the Solid-Water Interface*, John Wiely & Sons, Inc., New York, 1992.

33 P. Persson and K. Axe, *Geochem. Cosmochim. Acta*, 2005, 69, 541-552.

34 K. Mesuere and W. Fish, *Environ. Sci. Technol.*, 1992, 26, 2357-2364.

35 P. A. O'Day, *Rev. Geophys.*, 1999, 37, 249-274.

36 G. Bondietti, J. Sinniger and W. Stumm, *Colloids Surf. A.*, 1993, 79, 157-167.

37 W. Stumm, *Colloids Surf. A.*, 1997, 21, 143-166.

38 R. Kummert and W. Stumm, *J. Colloid Interface Sci.* , 1980, 75, 373-385.

39 L. S. Balistrieri and J. W. Murray, *Geochem. Cosmochim. Acta*, 1987, 51, 1151-1160.

40 P. Cambier and G. Sposito, *Clay Miner.*, 1991, 39, 369-374.

41 C. R. Evanko and D. A. Dzombak, *J. Coll. Inter. Sci.*, 1999, 214, 189-206.

42 D. A. Sverjensky and K. Fukushi, *Environ. Sci. Technol.*, 2006, 40, 263-271.

43 J. A. Davis, R. O. James and J. O. Leckie, *J. Colloid Interface Sci.*, 1978, 63, 480-499.

44 A. Herbelin and J. C. Westall, 1999, FITEQL: A Computer Program for Determination of Chemical Equilibrium Constants from Experimental data. Rep. 6-01, Version 04.00, Dept. of Chemistry, Oregon State Univ., Corvallis, OR.

45 J. Tofan-Lazar, A. Situm and H. A. Al-Abadleh, *J. Phys. Chem. A*, 2013, 117, 10368-10380.

46 G. B. Deacon and R. J. Phillips, *Coor. Chem. Rev.*, 1980, 33, 227-250.

47 I. A. Mudunkotuwa and V. H. Grassian, *J. Am. Chem. Soc.*, 2010, 132, 14986-14994.

48 C. H. Specht and F. H. Frimmel, *Phys. Chem. Chem Phys.*, 2001, 3, 5444-5449.

49 H. G. M. Edwards and N. C. Russell, *J. Molec. Struc.*, 1998, 443, 223-231.

50 K. Nakamoto, J. Fujita, S. Tanaka and M. Kobayashi, *J. Am. Chem. Soc.*, 1957, 79, 4904-4908.

51 E. Mentasti and E. Pelizzetti, *J. Chem. Soc., Dalton Trans.*, 1973, 2605-2608.

52 S. E. Lappi, B. Smith and S. Franzen, *Spectrochim. Acta A.*, 2004, 60, 2611-2619.

53 I. V. Chernyshova, S. Ponnurangam and P. Somasundaran, *Phys. Chem. Chem Phys.*, 2013, 15, 6953-6964.

54 G. Lefevre, *Adv. Coll. Inter. Sci.*, 2004, 107, 109-123.

55 E. J. Elzinga and D. L. Sparks, *J. Coll. Inter. Sci.*, 2007, 308, 53-70.

56 J. D. Kubicki, K. W. Paul, L. Kabalan, Q. Zhu, M. K. Mrozik, M. Aryanpour, A.-M. Pierre-Louis and D. R. Strongin, *Langmuir*, 2012, 28, 14573-14587.

57 S. J. Hug, *J. Coll. Inter. Sci.*, 1997, 188, 415-422.

58 C. M. Eggleston, S. J. Hug, W. Stumm, B. Sulzberger and M. D. S. Afonso, *Geochem. Cosmochim. Acta*, 1998, 62, 585-593.

59 J.-F. Boily and A. Shchukarev, *J. Phys. Chem. C.*, 2010, 114, 2613-2616.

60 K. Shimizu, A. Shchukarev, P. A. Kozin and J.-F. Boily, *Surf. Sci.*, 2012, 606, 1005-1009.

61 K. Shimizu, A. Shchukarev, P. A. Kozin and J.-F. Boily, *Langmuir*, 2013, 29, 2623-2630.

62 S. Kerisit, E. S. Ilton and S. C. Parker, *Journal of Physical Chemistry B*, 2006, 110, 20491-20501.

63 B. J. Finlayson-Pitts, *Phys. Chem. Chem. Phys.*, 2009, 11, 7760-7779.

64 A. W. Adamson, *Physical Chemistry of Surfaces*, John Wiley & Sons, New York, 5th edn., 1990.

65   S. C. B. Myneni, S. J. Traina, G. A. Waychunas and T. J. Logan, *Geochim. Cosmochim. Acta*, 1998, 62, 3285-3300.

66   O. Duckworth and S. T. Martin, *Geochem. Cosmochim. Acta*, 2001, 65, 4289-4301.

67   C. A. Lanzl, J. Baltrusaitis and D. M. Cwiertny, *Langmuir*, 2012, 28, 15797-15808.

68   T. Echigo, D. M. Aruguete, M. Murayama and M. F. Hochella Jr., *Geochem. Cosmochim. Acta*, 2012, 90, 149-162.

69   S. Chatman, P. Zarzycki and K. M. Rosso, *Phys. Chem. Chem Phys.*, 2013, 15, 13911-13921.

One sentence on novelty of the work (20 words max.):

In situ molecular-level infrared spectroscopic analysis coupled with surface complexation

modeling of organics at the aqueous solution-hematite nanoparticle interface.

TOC Graphic